frontiers | Frontiers in Earth Science

ORIGINAL RESEARCH
published: 03 May 2022
doi: 10.3389/feart.2022.799328

Investigating Nanoscale Electron Transfer Processes at the Cell-Mineral Interface in Cobalt-Doped Ferrihydrite Using *Geobacter sulfurreducens*: A Multi-Technique Approach

*Dawn M. Buchanan[1], Laura Newsome[2], Jonathan R. Lloyd[1], Majid Kazemian[3], Burkhard Kaulich[3], Tohru Araki[3], Heath Bagshaw[4], John Waters[1], Gerrit van der Laan[3], Alpha N'Diaye[5] and Victoria S. Coker[1]**

[1]Department of Earth and Environmental Sciences, University of Manchester, Manchester, United Kingdom, [2]Camborne School of Mines and Environment and Sustainability Institute, University of Exeter, Exeter, United Kingdom, [3]Diamond Light Source, Didcot, United Kingdom, [4]Albert Crewe Centre for Electron Microscopy, School of Engineering, University of Liverpool, Liverpool, United Kingdom, [5]Advanced Light Source, Lawrence Berkeley National Laboratory, Berkeley, CA, United States

OPEN ACCESS

Edited by:
Kevin Rosso,
Pacific Northwest National Laboratory (DOE), United States

Reviewed by:
Drew E. Latta,
The University of Iowa, United States
Maria Dittrich,
University of Toronto Scarborough, Canada

***Correspondence:**
Victoria S. Coker
vicky.coker@manchester.ac.uk

Specialty section:
This article was submitted to Geochemistry, a section of the journal Frontiers in Earth Science

Received: 21 October 2021
Accepted: 22 March 2022
Published: 03 May 2022

Citation:
Buchanan DM, Newsome L, Lloyd JR, Kazemian M, Kaulich B, Araki T, Bagshaw H, Waters J, van der Laan G, N'Diaye A and Coker VS (2022) Investigating Nanoscale Electron Transfer Processes at the Cell-Mineral Interface in Cobalt-Doped Ferrihydrite Using Geobacter sulfurreducens: A Multi-Technique Approach. Front. Earth Sci. 10:799328. doi: 10.3389/feart.2022.799328

Cobalt is an essential element for life and plays a crucial role in supporting the drive to clean energy, due to its importance in rechargeable batteries. Co is often associated with Fe in the environment, but the fate of Co in Fe-rich biogeochemically-active environments is poorly understood. To address this, synchrotron-based scanning X-ray microscopy (SXM) was used investigate the behaviour of cobalt at the nanoscale in Co-Fe(III)-oxyhydroxides undergoing microbial reduction. SXM can assess spatial changes in metal speciation and organic compounds helping to elucidate the electron transfer processes occurring at the cell-mineral interface and inform on the fate of cobalt in redox horizons. *G. sulfurreducens* was used to reduce synthetic Co-ferrihydrite as an analogue of natural cobalt-iron-oxides. Magnetite [$Fe(II)/Fe(III)_3O_4$] production was confirmed by powder X-ray diffraction (XRD), SXM and X-ray magnetic circular dichroism (XMCD) data, where best fits of the latter suggested Co-bearing magnetite. Macro-scale XAS techniques suggested Co(III) reduction occurred and complementary SXM at the nanoscale, coupled with imaging, found localised biogenic Co(III) reduction at the cell-mineral interface *via* direct contact with outer membrane cytochromes. No discernible localised changes in Fe speciation were detected in the reordered cobalt-iron-oxides that were formed and at the end point of the experiment only 11% Co and 1.5% Fe had been solubilised. The solid phase retention, alongside the highly localised and preferential cobalt bioreduction observed at the nanoscale is consistent with retention of Co in redox zones. This work improves our fundamental molecular-scale understanding of the fate of Co in complex environmental systems and supports the development of biogenic Co-doped magnetite for industrial applications from drug delivery systems to magnetic recording media.

Keywords: cobalt, ferrihydrite, polymetallic nodules, magnetite, scanning transmission X-ray microscopy

INTRODUCTION

Cobalt is designated a critical metal by the EU (European Commission, 2017) with increasing demand coming from industrial applications including superalloys for the aerospace industry (Shedd, 2015; Pollock, 2016; Slack et al., 2017), 'permanent' magnets for military and industrial applications (Tkaczyk et al., 2018) as well as its central role in rechargeable battery technology (Hein & Koschinsky, 2013; Hein et al., 2015; Shedd, 2015). Typically, cobalt is mined from minerals such as sulphosalt cobaltite [$(Co_2Fe)As$], heterogenite [$HCoO_2$] and Co-rich asbolane [$(Ni, Co)_xMn(IV)\ (O,OH)_4 \bullet nH_2O$] (Smith, 2001; Vanbrabant et al., 2013; Burlet and Vanbrabant, 2015; Dehaine et al., 2021); however, cobalt can also be found associated with ferrihydrite in soil sediments (Woodward et al., 2018) and polymetallic nodules (Mizell and Hein, 2018) and these have been identified as potential new sources of cobalt. In addition, anthropogenic activities, such as mining (Sharma and Agrawal, 2005), have led to increases in heavy metal pollution in soils and sediments. Cobalt is an essential nutrient in trace quantities, however, at elevated concentrations cobalt is known to cause physiological problems, such as insufficient chlorophyll production in plants and respiratory/cardiac diseases in mammals (Agency for Toxic Substances and Disease Registry, 2004; Slack et al., 2017; Woodward et al., 2018).

Cobalt is typically released to the environment as either Co(II) or Co(III) (Kosiorek and Wyszkowski, 2019), however, it is most commonly found as Co(II), the more thermodynamically stable species (Faucon et al., 2007; Newsome et al., 2020; Dehaine et al., 2021). Co(II) can be oxidised to Co(III) by Fe(III)-bearing minerals (Cornell and Giovanoli, 1989; Zachara et al., 2001; Pozas et al., 2004; He et al., 2020) and substituted into the crystal lattice of minerals such as goethite (Bousserrhine et al., 1999); as such, the fate of Co in the environment and the behaviour of Fe are intertwined (Fredrickson et al., 2001; Zachara et al., 2001; Grybos et al., 2007; Poggenburg et al., 2016). Ferrihydrite, an Fe(III)-oxyhydroxide ubiquitous in the environment, is characterised by its nanoparticulate nature, poor crystallinity, low stability and high dispersion (Dritus et al., 1992; Yee et al., 2006; Cismasu et al., 2016). Ferrihydrite has a high surface area and can readily sorb to the surface, or substitute small quantities of trace metals, such as Co, within the mineral structure (Cornell and Giovanoli, 1989; Kukkadapu et al., 2004). Co(III) [0.0545 nm] has a similar ionic radius to Fe(III) [0.0645 nm]; this, along with the valency of the cobalt ions and their electronic properties, in comparison to high-spin Fe(III), allows isomorphic substitution thus explaining the environmental occurrence of cobalt-iron-oxides (Zachara et al., 2001).

Polymetallic nodules, also known as ferromanganese nodules, are formed hydrogenetically, where seawater is the exclusive source of the metals (Valsangkar et al., 1992; Atkins et al., 2014), or diagenetically, where metals are supplied from pore waters of seafloor sediments (Nitahara et al., 2017; Maciąg et al., 2019). Hydrogenetic nodules are typically enriched in Co, Te, platinum group metals (PGM) plus rare earth elements (REEs), while diagenetic nodules are enriched in Ni, Cu, Mn, and Li (Hein and Koschinsky, 2013). Most nodules, however, have a hybrid origin (Mohwinkel et al., 2014; Mizell and Hein 2018) and Co enrichment in these has been documented (Banakar, 2010; Marsh et al., 2013; Mohwinkel et al., 2014; Josso et al., 2017; Petavratzi et al., 2019), hosted within the structure of poorly crystalline Fe minerals such as ferrihydrite (Mizell and Hein, 2018). Polymetallic nodules contain an untapped cobalt resource yet there is currently no economically viable industrial scale cobalt extraction process (Petavratzi et al., 2019). The demand for cobalt, combined with concerns regarding future supply, has encouraged governments to investigate alternative sources of this critical raw metal and to improve our understanding of the biogeochemical cycling of cobalt (Naden, 2017). Furthermore, the fate and mobility of cobalt from Co-ferrihydrite warrants further investigation to aid in the development of novel remediation practices (Woodward et al., 2018).

A wide phylogenetic range of microorganisms are capable of dissimilatory Fe(III) reduction, with *Shewanella* and *Geobacter* species being the most rigorously investigated (Han et al., 2018). *Geobacter sulfurreducens*, a model dissimilatory metal-reducing bacterium, can couple the enzymatic reduction of Fe(III)-(oxyhydr)oxides to the oxidation of organic matter (e.g. Lovley et al., 1987; Lloyd, 2003; Weber et al., 2006; Newsome et al., 2018; Kappler et al., 2021) releasing aqueous Fe(II) (Lloyd, 2003; Lovley et al., 2004). Dissimilatory metal-reducing bacteria can also liberate trace metals such as Cr, Ni and Co associated within oxidised mineral phases, such as ferrihydrite (Lee et al., 2001; Lloyd, 2003; Zhang and Cheng, 2007; Joshi et al., 2018). In the absence of an electron shuttle, *G. sulfurreducens* preferentially performs this electron transfer process *via* a direct contact mechanism, mediated by outer membrane multiheme *c*-type cytochromes localised to the cell surface (Lloyd, 2003; Lovley et al., 2004; MacDonald et al., 2011; Malvankar et al., 2011; Levar et al., 2016; Newsome et al., 2018) with extracellular pili also recently implicated in electron transfer (Lovley and Walker, 2019). Previous work has shown that ferrihydrite can be reductively transformed by dissimilatory metal-reducing bacteria (Dritus et al., 1992; Caccavo et al., 1994; Fredrickson et al., 2001; Pattrick et al., 2002; Hansel et al., 2003; Weber et al., 2006; Coker et al., 2007; Li et al., 2012; Han et al., 2018; Newsome et al., 2018; Kappler et al., 2021) to magnetite (Lovley, 1987; Pattrick et al., 2002), a ferrite spinel with industrial applications such as drug delivery systems and magnetic recording media (Coker et al., 2009). The transformation of ferrihydrite to magnetite occurs *via* a dissolution, adsorption and reprecipitation reaction (e.g., Fredrickson et al., 2001; Hansel et al., 2003; Weber et al., 2006; Newsome et al., 2018; Kappler et al., 2021). During microbial transformations, cobalt associated with ferrihydrite may become incorporated into new reduced cobalt-bearing minerals (Coker et al., 2009; Byrne et al., 2013). Therefore an improved understanding of the fate of cobalt and electron transfer processes occurring between microbes and metals at the cell-mineral interface during the bioreduction of Co-ferrihydrite is necessary to better understand cobalt cycling in environmental systems.

In this study, we investigated the behaviour of cobalt during the enzymatic reduction of a synthetic Co-ferrihydrite using *G.*

sulfurreducens, as an analogue to bioreduction processes in the natural environment. Using a combination of geochemical measurements, electron microscopy, powder X-ray diffraction (PXRD) and X-ray absorption spectroscopy (XAS), changes in metal speciation and mineral phases were identified. Synchrotron-based scanning X-ray microscopy (SXM) was used to map elemental and chemical information for both bacteria and mineral phases by directly measuring at the C *K*-edge and the transition metal $L_{2,3}$-edges, with a high spatial (<40 nm; (Chao et al., 2012; Karunakaran et al., 2015)) and spectral resolution (0.1 eV; (Xia et al., 2013; Karunakaran et al., 2015)). SXM suggested highly localised Co(III) reduction in regions co-located with bacterial cells; however, no spatial changes in Fe speciation were observed. Analyses also suggested a high degree of solid phase cobalt and iron retention, despite a change to a more reduced mineral phase. These data can be extrapolated to understand the natural biogeochemical cycling of cobalt in Fe-rich environments undergoing microbially-mediated redox transformations.

MATERIALS AND METHODS

Synthesis and Characterisation of Cobalt-Doped Ferrihydrite

Cobalt-doped 2-line ferrihydrite was prepared according to a method adapted from Cornell and Schwertmann (2003). Briefly, using a stirring plate, 20 g of iron (III) chloride hexahydrate ($FeCl_3.6H_2O$) and 3.1 g of cobalt (II) chloride hexahydrate ($CoCl_2.6H_2O$) was dissolved in 500 ml of deionised water. 10 M NaOH was used to increase the pH from 1.7 to 6.9 and the subsequent mineral precipitate was washed five times using de-ionised water. The mineral precipitates were then resuspended in 200 ml deionised water and stored at 4°C.

The mineral composition of the final solids was confirmed using (powder) X-ray diffraction (PXRD). A Bruker D8Advance instrument with anti-scatter slits opened to 3° and a scanning range of 10°–70° (2θ), using a step size of 0.02° (2θ) was used to characterise the mineralogy of key time points in the biogenic reduction reaction. The International Centre for Diffraction Data database; PDF4 Mineral 2021 package was used to analyse the data.

An aliquot of the final synthesized mineral was acidified in 2 w/v % HNO_3 to determine the concentration of Fe and Co using inductively coupled plasma atomic emission spectroscopy (ICP-AES, PerkinElmer Optima 5,300 dual view), located in a clean laboratory environment (Class 1,000) at the Manchester Analytical Geochemistry Unit.

Culturing *Geobacter sulfurreducens*

G. sulfurreducens was obtained from the laboratory culture collection of the Geomicrobiology Group in the Williamson Centre for Molecular Environmental Science at the University of Manchester. Standard methods regarding culturing and strict anaerobic preparation of cells of *G. sulfurreducens* were followed as described previously (Lloyd 2003). The cultures were grown at 30°C in modified fresh water medium with sodium acetate (10 mM) and fumarate (40 mM) as the electron donor and acceptor, respectively. All manipulations were carried out under an atmosphere of N_2-CO_2 (80:20). Late logarithmic phase cultures of *G. sulfurreducens* were harvested by centrifugation at 4°C (5,000 *g*; 20 min) and washed three times in sodium bicarbonate buffer ($NaHCO_3$; 30 mM, pH 7.1) under N_2-CO_2 (80:20) prior to use.

Experimental Procedure

An anaerobic stock solution of Co-ferrihydrite in 10 mM sodium bicarbonate buffer was prepared, yielding a slurry of 2 mmol/L Fe at circum-neutral pH. The experimental samples contained 5 ml of the anaerobic stock solution, 10 mM sodium acetate (the electron donor) and an aliquot of the cell suspension, washed to achieve a final optical density (OD_{600}) of 0.6 (Jenway 6,715 series UV-vis spectrophotometer). Experiments were conducted in triplicate unless stated otherwise. All sample bottles were incubated in the dark at 30°C.

Experiments were monitored at 1, 9, 20, and 72 h. The ferrozine assay (Stookey, 1970) was used to measure the concentration of Fe(II) and total bioavailable Fe [Fe (tot)] by digestion of sample aliquots (suspension samples taken from well shaken bottles) in 0.5 M HCl for 1 h to measure Fe(II) and the addition of 0.25 M hydroxylamine hydrochloride for total Fe. Aliquots of sample suspensions were centrifuged (5 min; 16,000 *g*) and the supernatant was acidified for ICP-AES and inductively coupled plasma mass spectrometry (ICP-MS, VG Elemental Plasmaquad 2 STE) to monitor the concentration of Fe and Co in the aqueous phase, respectively.

At corresponding timepoints, samples were prepared for characterisation by spectroscopy and microscopy. One sample bottle was opened under a nitrogen atmosphere and 2 µl aliquots were mounted on carbon-coated Cu grids for transmission electron microscopy (TEM) and SXM analyses. The remaining sample slurry was dried under nitrogen, where a portion was attached to carbon tape on a copper holder and maintained in an anaerobic environment for bulk $L_{2,3}$ edge XAS analysis while the remainder was used for PXRD analysis.

Transmission Electron Microscopy (TEM)

A FEI Tecnai T20 (200 kV LaB6) instrument fitted with a X-Max 80 SSD Energy Dispersive X-ray analysis (EDS) system (Oxford Instruments; Aztec software) using a Gatan Orius SC200 CCD camera (Gatan GMS 2 software) was used to observe the interactions between the microbial cells and new mineral phases produced by *G. sulfurreducens*. The resultant TEM images are bright-field images.

X-ray Magnetic Circular Dichroism (XMCD)

Fe $L_{2,3}$ edge X-ray magnetic circular dichroism (XMCD) spectra were collected on beamline 6.3.1 at the Advanced Light Source (ALS), Berkeley, United States, using a spot size of 180 µm × 80 µm (Lawrence Berkeley National Laboratory, 2021) in total-electron yield (TEY) mode with an analysis depth of ~4.5 nm (van der Laan and Thole, 1991; Coker et al., 2007). The samples were orientated central to the magnetic pole pieces to allow the X-ray beam to enter through a hole parallel and anti-parallel to the

magnetic field and perpendicular to the sample surface (Coker et al., 2007). Scanning between 705–730 eV, the Fe $L_{2,3}$ edge XAS data were collected for the two opposite magnetisation directions, and then normalised to the incident beam intensity and subtracted from each other to give the XMCD spectrum (Pattrick et al., 2002).

XMCD was used to determine the site occupancy of Fe cations in the biogenic mineral phases (Coker et al., 2007). To obtain the relative amounts of the three Fe sites: Fe d^6 O_h, d^5 T_d and d^5 O_h; the experimental spectra were fitted by means of a non-linear least-squares analysis as reported in Coker et al. (2007), using calculated spectra for each of the Fe sites provided by van der Laan and Thole (1991).

Bulk $L_{2,3}$ Edge X-ray Absorption Spectroscopy (XAS)

Bulk Mn and Co $L_{2,3}$ edge X-ray absorption spectroscopy (XAS) data were collected on beamline 6.3.1 at the Advanced Light Source (ALS), Berkeley, United States using TEY giving a typical analysis depth of ~4.5 nm into the sample (Coker et al., 2009). The experimental spectra were normalised to the incident beam.

Scanning X-ray Microscopy (SXM)

Scanning X-ray microscopy (SXM) data were collected at the Diamond Light Source (DLS), UK, on beamline I08 using a 25 nm Fresnel zone plate lens. Experimental spectra were calibrated to the C 1*s*-π* transition associated with carbonyl carbon in amide moieties present in proteins (Lawrence et al., 2003; Cody et al., 2008; Coker et al., 2012) and at the Fe and Co $L_{2,3}$-edges using the Fe(II) peak at 708.7 eV (Bourdelle et al., 2013; Hawkings et al., 2018) and the Co(III) peak at 780.6 eV (Istomin et al., 2015). Image sequences (stacks), were collected at prescribed intervals over the relevant absorption edges, that is, C *K* edge: 280–310 eV, Fe $L_{2,3}$ edge: 700–735 eV and Co $L_{2,3}$ edge: 770–805 eV, with smaller increment steps at the L_3 edge to increase spectral sensitivity over this quantitative edge (Pattrick et al., 2002). To minimise beam damage, SXM data were obtained in order of increasing photon energies. Furthermore, dwell times $\leqslant$ 5 ms were used and the shutter remained closed when data were not being gathered. No radiation damage was observed under these experiment conditions.

The 'Jacobson stack analyse' function (Jacobsen et al., 2000) from the "aXis2000" software (Hitchcock, 2011) was used to align the transmission images in the stacks. Sample free areas of the carbon film Cu grids were used to normalize the transmission signal obtained from analysed regions of interest. Transmission images from the stacks were converted to optical density (OD) images according to Beer-Lambert's law (Eq. 1), where I_0 is the incident photon intensity and I the transmitted intensity (Moffet et al., 2011).

$$\mathrm{OD} = \ln\left(\frac{I_0}{I}\right)$$

Eq. 1. Beer-Lambert's law.

To monitor spatial and temporal changes in metal speciation, Fe and Co $L_{2,3}$-edge SXM spectral measurements

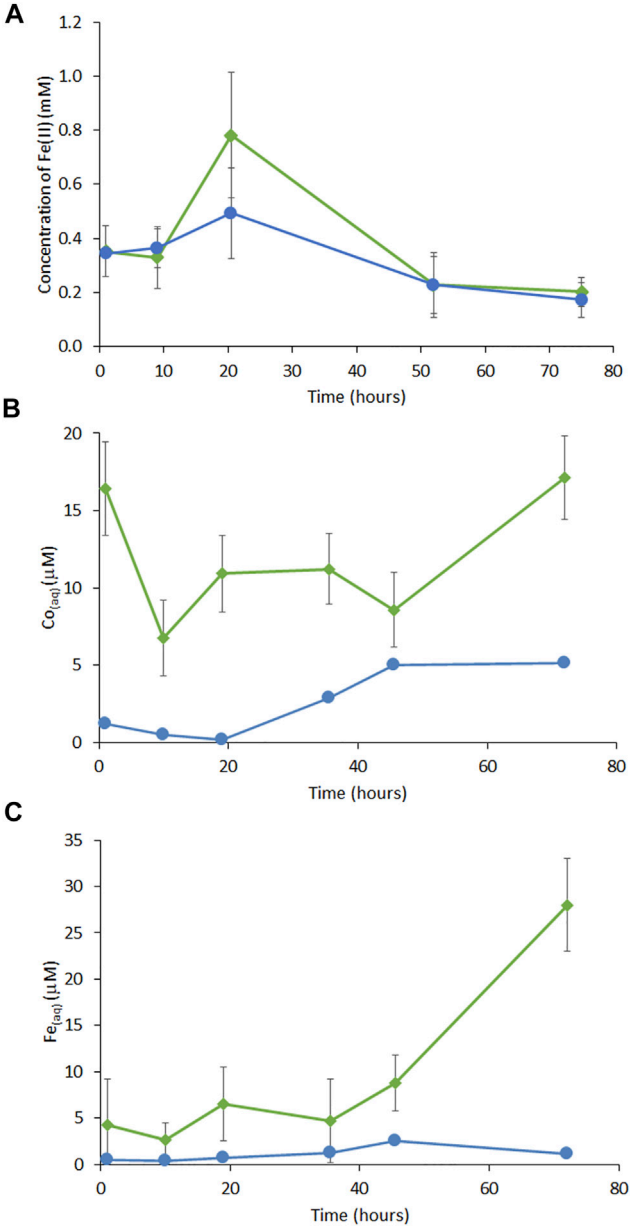

FIGURE 1 | (A) Concentration of Fe(II) from measurement of 0.5 M HCl digestion of slurry by ferrozine assay, **(B)** ICP-MS monitoring of aqueous phase Co and **(C)** ICP-AES monitoring of aqueous Fe in Co-doped ferrihydrite with *G. sulfurreducens* (green lines) and no electron donor controls (blue lines). Error bars are ±1 standard deviation.

were fitted by means of a non-linear least-squares analysis using calculations for Fe(II), Fe(III), Co(II) and Co(III) in octahedral coordination (**Supplementary Figure S1**) to determine the proportion of each metal species as described previously by van der Laan and Thole (1991). Spectral modelling of this nature has been shown to give quantitative results at the L_3 peak while the L_2 peak notes a qualitative agreement (Pattrick et al., 2002). Interpretation of spectra *via* this method has its limitations as the experimental

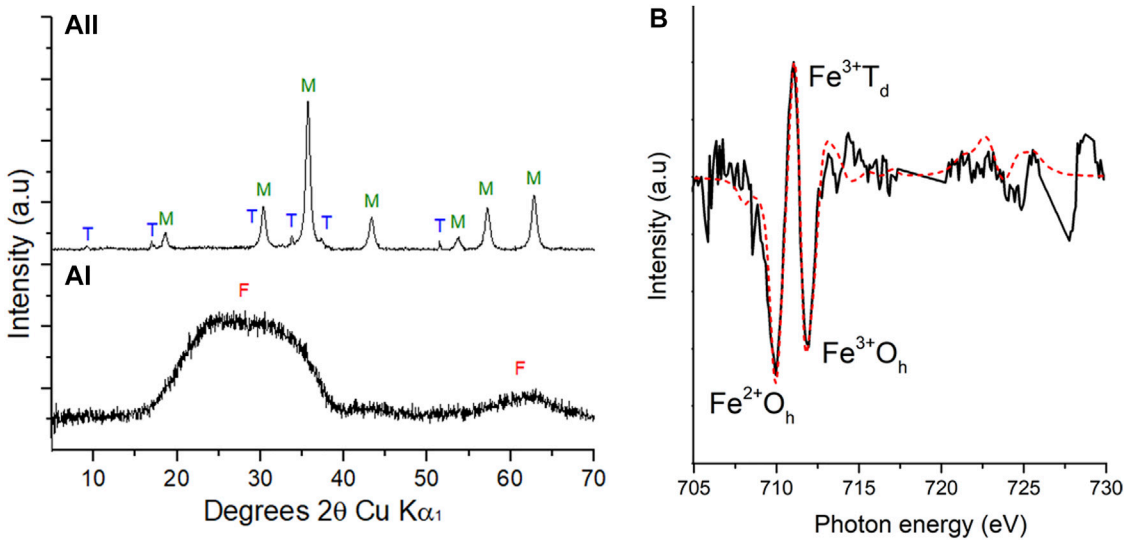

FIGURE 2 | PXRD patterns **(A)** during the bioreduction of cobalt doped ferrihydrite by *G. sulfurreducens* from 0 h (a(I)) and 9 h (a (II)). F: ferrihydrite, M: magnetite, T: Trona. Fe $L_{2,3}$ XMCD **(B)** experimental (solid line) spectrum and best fit (red dashed line) calculated spectrum based on the three theoretical site components listed in **Table 1** for XMCD at 9 h.

spectra can be altered (e.g., Jahn–Teller distortion (van der Laan and Kirkman, 1992; Glatzel et al., 2005), consequently, the values of each metal species have a 10% error (Coker et al., 2009).

Fe $L_{2,3}$-edge images stacks collected at the 9 and 20 h timepoints had multiple regions of interest that were too thick to facilitate transmission, producing broad spectra due to oversaturation. Masks comprised of pixels from regions of appropriate thickness were prepared using the 'aXis2000' software (Hitchcock, 2011) to correct for this. The spectra from these masks were used alongside the aggregate SXM spectra, prepared from averages from the regions analysed.

RESULTS

Bulk Characterisation

Cobalt-ferrihydrite, with a final molar ratio of 1:0.12 Fe:Co, was subjected to bioreduction by *G. sulfurreducens* Elevated Fe(II) was detected in experimental samples where up to 0.8 mM Fe(II) (40% of total Fe) was found in the cell-mineral suspension by the ferrozine assay (**Figure 1A**). Minor Co release was associated with the addition of *G. sulfurreducens* with 17 μM released in the experiment samples compared to 5.2 μM in the control at the final timepoint (**Figure 1B**). At the final timepoint, 28 μM Fe had been released to solution in the experiment samples versus a negligible release (1.1 μM) in the no electron donor control (**Figure 1C**).

PXRD confirmed a starting material of 2-line ferrihydrite with broad peaks between 20° and 40° (2θ) and 60°–65° (2θ) (**Figure 2A**(I)). Magnetite ($Fe(II)Fe(III)_2O_4$), a magnetic Fe(II)-bearing mineral phase, dominated from 9 h (**Figure 2A**(II))) with residual peaks attributed to trona ($Na_3H(CO_3)_2{\cdot}2H_2O$), a hydrated sodium bicarbonate, confirming a bioreduction process had occurred.

Fe $L_{2,3}$ edge XAS data were collected in opposing magnetic fields and subtracted to give XMCD spectra for the 9 h sample shown here in **Figure 2B** with best fits derived from the calculated spectra (van der Laan and Thole, 1991). These data evaluated the magnetic component of the samples, therefore only the magnetite, and noted an Fe(II):Fe(III) ratio of 0.46, similar to stoichiometric magnetite (0.50) and slightly less Fe(II) than previous samples (Coker et al., 2007) of pure biogenic magnetite (0.55) (**Table 1**). Normalising the data to Fe(III) O_h equal to 1 (**Table 1**), an estimate of the chemical formula for the Co-substituted ferrite can be obtained of $Co_{0.38}Fe_{2.73}O_4$, which is the difference between the fit for the experimental data compared to that for biogenic magnetite from previous work (Coker et al., 2009).

Transmission Electron Microscopy

Transmission electron microscopy (TEM) images were taken at 1, 9, 20 and 72 h. At 1 h *G. sulfurreducens* cells (1.5 μm) were observed closely associated with electron dense clumps of small nano-particles (~2 nm) (**Figure 3A**) and feather-like structures (1.5 μm) (**Figure 3B**). At 9 h the feather-like structures (0.75–1 μm) (**Figure 3C**) remained present, as well as dense aggregated particulates (~1 μm) (**Figure 3D**) which dominated. Bacterial rods remained in contact with the mineral phases; these two structures were likely the hydrated sodium bicarbonate from the buffer solution and the magnetite, respectively, as identified by the PXRD in **Figure 2A**(II)). At 20 h, dense aggregated particulates (~1 μm) (**Figures 2E,F**) and feather-like structures 2 μm in length were again observed (**Figure 2F**). At the final time point at 72 h, local agglomerations of rounded granules ~0.3 μm in diameter were prominent (**Figure 2G**), with residual laths (100 nm) (**Figure 2H**). Here, the bacteria were no longer closely associated with the mineral phase.

TABLE 1 | Fe site occupancies for biogenic materials calculated from XMCD (**Figure 2B**). * From Coker et al. (2007).

Sample	Fe(II) O_h	Fe(III) T_d	Fe(III) O_h	Fe(II)/Fe(III)	T_d/O_h
Stoichiometric magnetite*	1.00	1.00	1.00	0.50	0.50
Reduced biogenic magnetite*	1.10	1.01	1.00	0.55	0.48
9 h	0.86	0.87	1.00	0.46	0.47

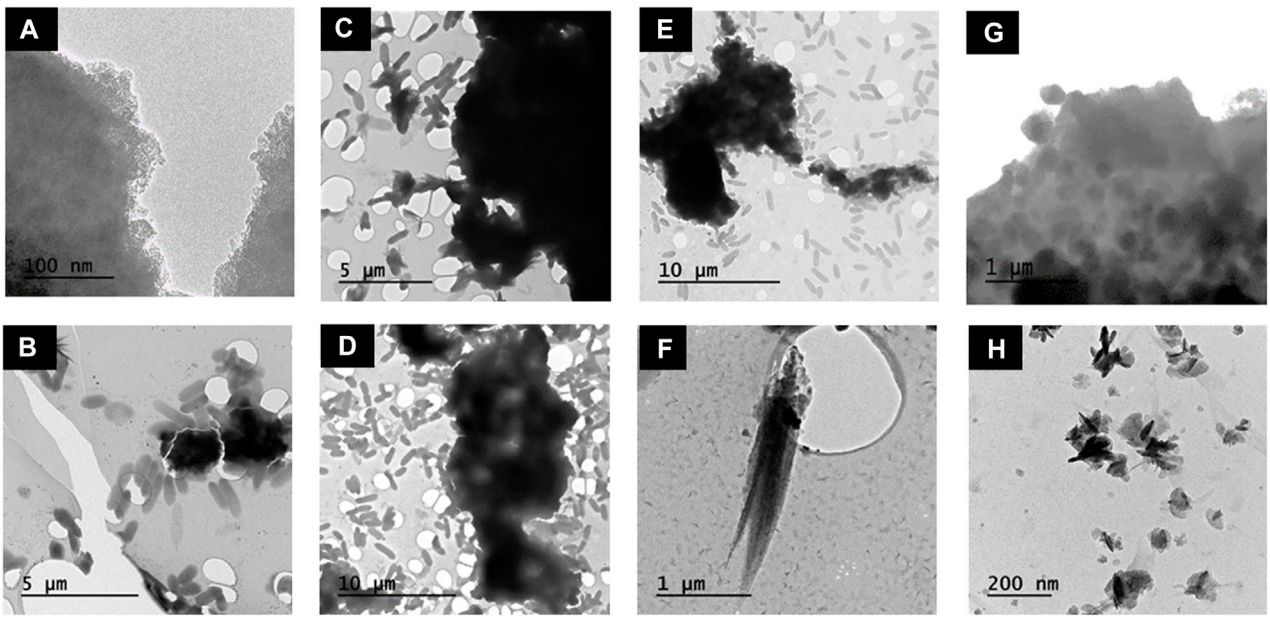

FIGURE 3 | TEM images of Co-doped ferrihydrite suspension associated with *G. sulfurreducens* and changes in mineral morphology over time. **(A,B)** 1 h; **(C,D)** 9 h; **(E–F)** 20 h; **(G–H)** 72 h.

Macro-scale Spectroscopy

Surface sensitive Fe and Co $L_{2,3}$ edge XAS (**Figure 4**) measurements were taken on a bulk homogenised powder of dried sample slurry measured in TEY mode; results showed a shift in the position of the main L_3 peak for both elements to lower photon energies over the course of the experiment, suggesting a change to a more reduced species (Glatzel et al., 2005). Modelling the Fe and Co $L_{2,3}$ edge, using calculated spectra for 2+ and 3+ species, indicated that the synthetic Co-doped ferrihydrite initially contained 76% Co(II) and 24% Co(III) and 100% Fe(III) (**Tables 2**, **3**). A marked difference was observed after 1 h where 88% Co(II) was detected as well as 21% Fe(II). The maximum proportion of Fe(II), 36%, occurred at 9 h and was maintained at 20 h. No bulk Fe data were available for the 72 h timepoint. At the final timepoint at 72 h, the proportion of Co(II) (90%) remained similar to that observed after 1 h (**Table 2**; **Figure 4**).

Co and Fe $L_{2,3}$-edge data from the areas analysed using SXM in transmission mode, called "aggregate SXM" data (see **Supplementary Table S1** for sample area and pixels used), are spatially constrained averages comparable to the surface sensitive bulk data (**Figure 4**; **Table 2**, **Table 3**). Aggregate Co $L_{2,3}$-edge SXM data showed excellent agreement with the bulk data suggesting a Co(II)-rich end point to the experiment (**Table 2**) and at corresponding timepoints, the proportions of Co(II) indicated by both XAS techniques were within 10% error (Coker et al., 2009). The aggregate Fe $L_{2,3}$-edge data, alike with the bulk data, showed a significant change in Fe speciation at 1 h where 46% Fe(II) was detected by the former technique (**Table 3**). Fe $L_{2,3}$-edge aggregate SXM data noted a Fe(II):Fe(III) ratio of 50:50 at 9 h, again indicating a more reduced Fe-bearing mineral, such as magnetite (Coker et al., 2007).

SXM Mapping

Bacterial Cells

To spatially resolve the location of the bacterial cells relative to the mineral phases, C *K*-edge stack maps were produced at 288.2 eV, corresponding to a 1s-π* transition associated with carbonyl carbon in amide moieties associated with proteins (Lawrence et al., 2003; Cody et al., 2008; Coker et al., 2012). Images mapping the location of Fe and Co were produced at L_3-edge peak intensities for Fe (~710 eV) and Co (780.6 eV) and combined with the carbon map to create RGB composite images (**Figures 5–8**). The RGB images serve to identify mineral regions co-

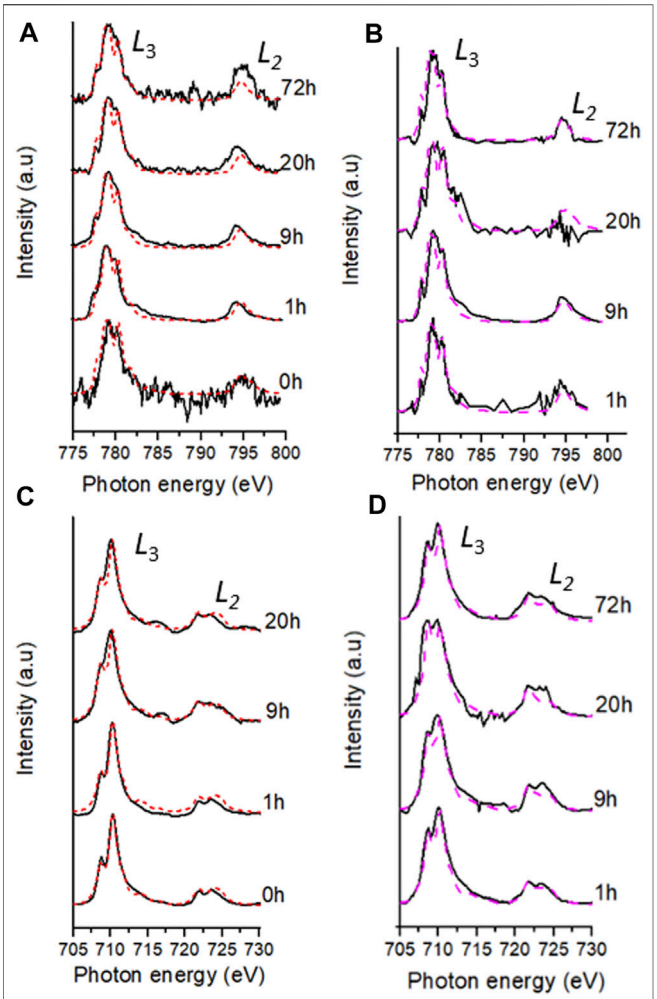

FIGURE 4 | Fe and Co best fits (dashed lines) of the experimental data (black lines) during the bioreduction of Co doped ferrihydrite suspension using *G. sulfurreducens* over 72 h; bulk $L_{2,3}$-edge XAS spectra (red lines) for Co **(A)** and Fe **(C)** and aggregate SXM data (pink lines) for Co **(B)** and Fe **(D)**.

located (X or EX if both Co and Fe were not measurable at the same location) with bacterial cells and regions not co-located (O) with bacterial cells. Fe and Co $L_{2,3}$-edge spectra from co-located and non-co-located points were modelled as above for the bulk data (**Supplementary Figure S2** and **Supplementary Figure S3**). Spectra from multiple regions of interest were analysed and the indicated proportions of metal speciation from the best fits were averaged (mean) (**Supplementary Table S2** and **Supplementary Table S3**). Using this nanoscale approach, significant changes in Co(II) speciation were observed (**Figure 9**).

Cobalt SXM

On average, at 1 h 82 ± 3.1% Co(II) was detected in non co-located regions and 89 ± 6.5% was detected in co-located regions (**Figure 9**; **Table 2**); therefore within experimental error (Coker et al., 2009). Analysis of the 9 h sample however detected 82 ± 2.1% Co(II) in the non co-located regions and a significant increase in the Co(II) proportion to 95 ± 7.4% in regions co-located with the bacterial cells (**Figure 9**; **Table 2**). In common with the 9 h sample, the 20 h sample also noted significantly more Co(II) in the mineral regions in close proximity to the cells with 74 ± 1.5% Co(II) detected in the non co-located regions and 85 ± 23.5% detected in the co-located regions (**Figure 9**; **Table 2**). Finally, at 72 h in regions co-located with the cells, the proportion of Co(II) increased significantly from 80 ± 1.8% to 97 ± 5% (**Figure 9**; **Table 2**).

Iron SXM

In contrast to the Co SXM data, a comparison of the Fe species between the non co-located and co-located regions at 1, 20 and 72 h showed no appreciable difference in Fe speciation either spatially or temporally after the 1 h timepoint, with 50 ± 2.7% Fe(II) found in co-located regions at the end point of the experiment (**Figure 10**; **Table 3**).

DISCUSSION

Rapid (< 1h) Formation of Co-Magnetite by *Geobacter sulfurreducens*

A higher concentration of Fe(II) and solubilised metals were measured in the experimental samples (**Figures 1A–C**), compared to the no electron donor control, demonstrating that the changes observed were due to enzymatic processes e.g., (Hansel et al., 2003; Han et al., 2018). During the

TABLE 2 | Summary of Co species proportions from key time points according to best fits using octahedral metal calculation for bulk $L_{2,3}$- edge data and average SXM data points. *Aggregate SXM,* spectra of the entire area imaged and analysed.

	Bulk XAS %		Aggregate SXM %		Average SXM: Non Co-located %		Average SXM: Co-located %	
Sample	Co(III)	Co(II)	Co(III)	Co(II)	Co(III)	Co(II)	Co(III)	Co(II)
t = 0 h	24	76	no data		no data		no data	
t = 1 h	12	88	13	87	18	82	11	89
t = 9 h	7	93	12	88	18	82	5	95
t = 20 h	15	85	23	77	26	74	15	85
t = 72 h	10	90	0	100	20	80	3	97

Average SXM: non co-located 1 h: average of 10 points. Average SXM: co-located 1 h: average of eight points. Average SXM: non co-located 9 h: average of 12 points. SXM: co-located 9 h: average of seven points. Average SXM: non co-located 20 h: average of five points. SXM: co-located 20 h: average of seven points. Average SXM: non co-located 72 h: average of 15 points. SXM: co-located 72 h: average of 14 points. There is a 10% error on all stated best fit values.

TABLE 3 | Summary of Fe species proportions from key time points according to best fits using octahedral metal calculation for bulk $L_{2,3}$- edge data and average SXM data points. *Aggregate SXM,* spectra of the entire area imaged and analysed.

	Bulk XAS %		Aggregate SXM %		Average SXM: Non Co-located %		Average SXM: Co-located %	
Sample	Fe(III)	Fe(II)	Fe(III)	Fe(II)	Fe(III)	Fe(II)	Fe(III)	Fe(II)
t = 0 h	100	0	no data		no data		no data	
t = 1 h	79	21	54	46	55	45	52	48
t = 9 h	64	36	50	50	no data		no data	
t = 20 h	68	32	41	59	52	48	54	46
t = 72 h	no data		52	48	56	44	50	50

Average SXM: non co-located 1 h: average of 10 points. Average SXM: co-located 1 h: average of nine points. Average SXM: non co-located 17 h: average of eight points. SXM: co-located 20 h: average of nine points. Average SXM: non co-located 72 h: average of 13 points. SXM: co-located 72 h: average of 15 points. There is a 10% error on all stated best fit values.

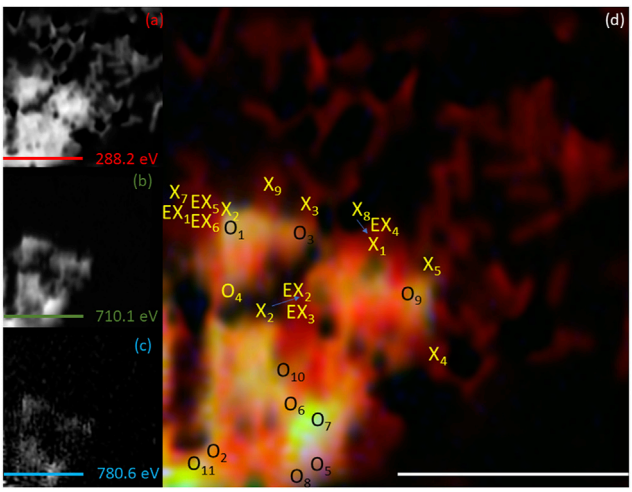

FIGURE 5 | Elemental maps for the 1 h timepoint for **(A)** C *K*-edge (288.2 eV; red), **(B)** Fe $L_{2,3}$-edge (710.1 eV; green) and **(C)** Co $L_{2,3}$-edge (780.6 eV; blue). The corresponding composite RGB (red, green, blue) image **(D)** shows the spatial relationship between the bacterial cells (C *K*-edge) and the minerals (Fe and Co $L_{2,3}$-edges). Spectra were taken from regions co-located with the bacterial cells (X or EX) and regions not co-located to the bacterial cell (O). The centre of the "X" and "O" denote the precise location from which the spectra were collected. All scale bars are 7 μm.

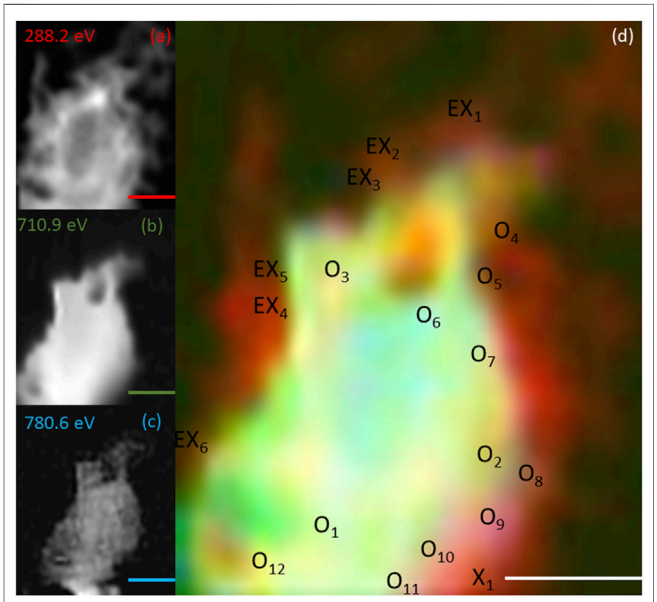

FIGURE 6 | Elemental maps for the 9 h timepoint for **(A)** C *K*-edge (288.2 eV; red), **(B)** Fe $L_{2,3}$-edge (710.9 eV; green) and **(C)** Co $L_{2,3}$-edge (780.6 eV; blue). The corresponding composite RGB (red, green, blue) image **(D)** shows the spatial relationship between the bacterial cells (C *K*-edge) and the minerals (Fe and Co $L_{2,3}$-edges). Spectra were taken from regions co-located with the bacterial cells (X) and regions not co-located to the bacterial cell (O). The centre of the 'X' and 'O' denote the precise location from which the spectra were collected. All scale bars are 2 μm.

experiment, Fe(II) initially increased (**Figure 1A**), which is indicative of reductive dissolution (Fredrickson et al., 2001; Hansel et al., 2003; Weber et al., 2006; Yang et al., 2010; Li et al., 2012; Newsome et al., 2018; Kappler et al., 2021). The aqueous Fe(II) then adsorbed to the surface of remaining ferrihydrite and induced the formation of magnetite, confirmed by PXRD, XMCD (**Figure 2**) and aggregate SXM (**Table 3**) and imaged using TEM. The removal of Fe(II) from solution during magnetite formation explained the limited extent of Fe in solution at the final timepoint (**Figure 1C**).

Co(III/II) can be substituted into the crystal lattice of Fe(III) minerals, such as goethite (Bousserrhine et al., 1999). During the enzymatic reduction and recrystallisation of the Co-bearing ferrihydrite, reductive dissolution of Fe(III) would prompt the release of incorporated Co(III/II), consistent with aqueous geochemistry observations (**Figure 1B**) (Lee et al., 2001; Lloyd, 2003; Zhang and Cheng, 2007; Joshi et al., 2018). Co(III) is a strong oxidising agent, and no stable dissociated Co(III) compounds exist in aqueous solution (Ma et al., 2008). It is therefore likely that the minor amount of solubilised cobalt at the end point is Co(II), which is the more thermodynamically stable species (Faucon et al., 2007; Newsome et al., 2020; Dehaine et al., 2021), highly soluble in water and potentially very mobile (Woodward et al., 2018). However, the majority of the Co remained associated with the solid phase during microbial reduction suggesting that the solubilised Co was reincorporated into the magnetite during Fe mineral recrystallisation, explaining the fluctuations in Co concentration (**Figure 1B**). Co(III) can be biotically reduced to

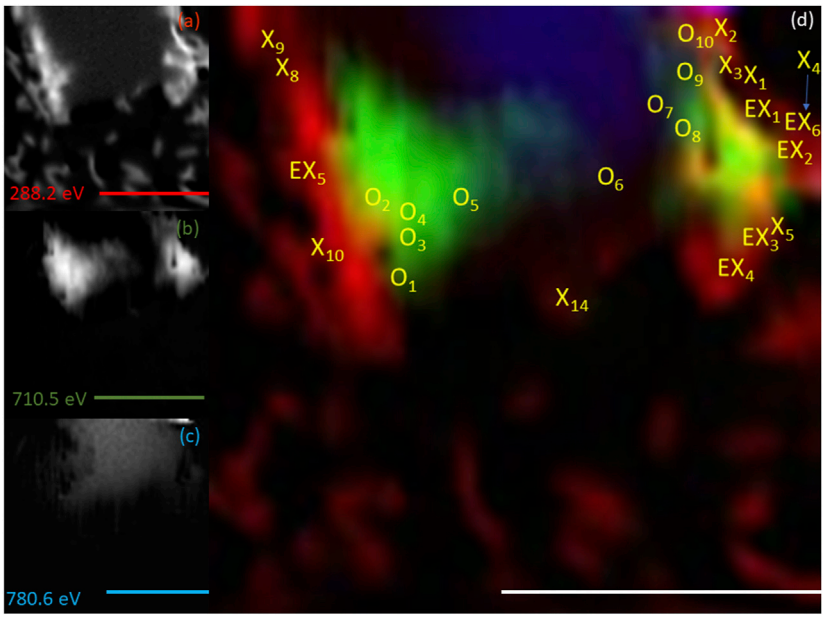

FIGURE 7 | Elemental maps for the 20 h timepoint for **(A)** C *K*-edge (288.2 eV; red), **(B)** Fe $L_{2,3}$-edge (710.5 eV; green) and **(C)** Co $L_{2,3}$-edge (780.6 eV; blue). The corresponding composite RGB (red, green, blue) image **(D)** shows the spatial relationship between the bacterial cells (C *K*-edge) and the minerals (Fe and Co $L_{2,3}$-edges). Spectra were taken from regions co-located with the bacterial cells (X) and regions not co-located to the bacterial cell (O). The centre of the 'X' and 'O' denote the precise location from which the spectra were collected. All scale bars are 7 μm.

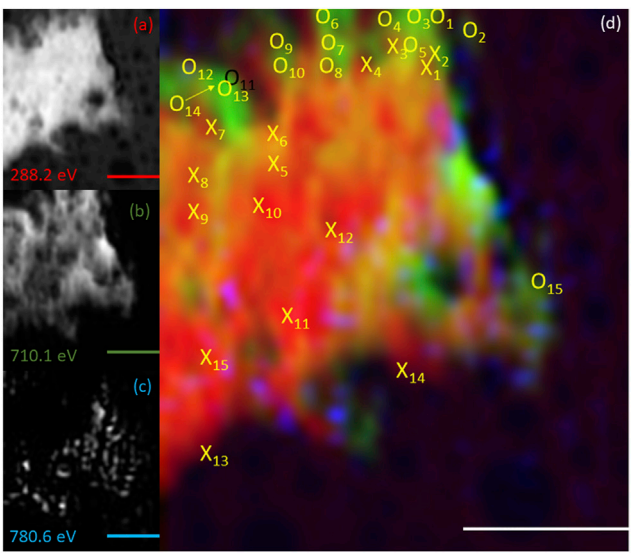

FIGURE 8 | Elemental maps for the 72 h timepoint for **(A)** C *K*-edge (288.2 eV; red), **(B)** Fe $L_{2,3}$-edge (710.1 eV; green) and **(C)** Co $L_{2,3}$-edge (780.6.0 eV; blue). The corresponding composite RGB (red, green, blue) image **(D)** shows the spatial relationship between the bacterial cells (C *K*-edge) and the minerals (Fe and Co $L_{2,3}$-edges). Spectra were taken from regions co-located with the bacterial cells (X) and regions not co-located to the bacterial cell (O). The centre of the 'X' and 'O' denote the precise location from which the spectra were collected. All scale bars are 3 μm.

Co(II) as first noted by Gorby, Caccavo and Bolton (1998) for Co(III)-EDTA, therefore the increased detection of Co(II) may have been due to the enzymatic reduction of Co(III) by *G. sulfurreducens*; however, from the macro scale spectroscopy it was not possible to determine the precise mechanism that was responsible for the increase in Co(II) detected. Borch *et al.* (2010) and Zachara *et al.* (2001) suggested that during reductive dissolution processes, Fe(II) mobilisation may be interrupted by the adsorption or coprecipitation of trace metals with the newly formed minerals. Therefore, Fe(II) mobilisation enabled the cobalt to become incorporated into the structure of the magnetite explaining the deficit at the Fe(II)O_h site, compared with biogenic magnetite (**Table 1**). This suggested that the solubilised Co(II) was reincorporated here, the expected site for Co substitution as seen previously (Wu et al., 2007; López et al., 2008; Coker et al., 2009).

Changes in Bulk Speciation of Co and Fe Over 72 h

During mineral synthesis, 24% (**Table 2**) of the cobalt(II) chloride hexahydrate ($CoCl_2.6H_2O$) was oxidised to Co(III) (0.545 Å, high spin configuration) and substituted for Fe(III) (0.645 Å, high spin configuration) (Zachara et al., 2001), due to similar ionic radii (Zachara et al., 2001; Pozas et al., 2004), forming the Co-ferrihydrite. The bulk Co $L_{2,3}$-edge XAS data noted an early significant increase in the proportion of Co(II), suggesting a rapid reduction of Co(III) producing a Co(II) rich mineral (**Table 2**). The spatially constrained aggregate SXM data showed excellent agreement with the bulk data, but noted a significant fluctuation in the proportion of Co(II) at 20 h (**Table 2**), highlighting

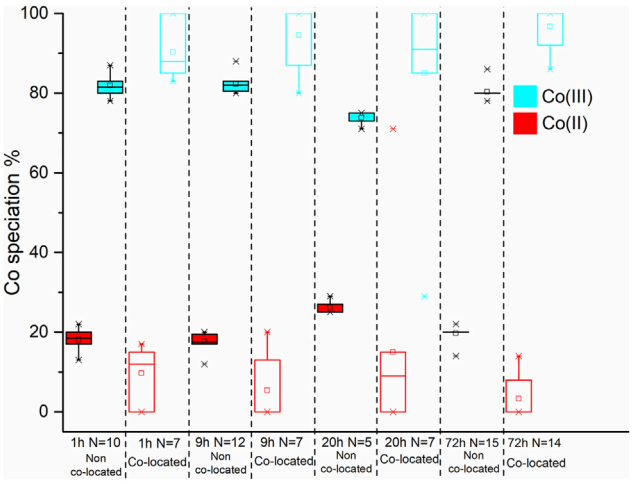

FIGURE 9 | Box and whisker plot diagrams showing the changes in Co speciation over the course of the experiment. The box and whisker plots for the starting material have a dotted outline. The box and whisker plots from the non co-located regions have a solid black outline while those from the co-located regions have coloured outline. In both spatial regions the Co(III) and Co(II) data is represented with red and blue, respectively.

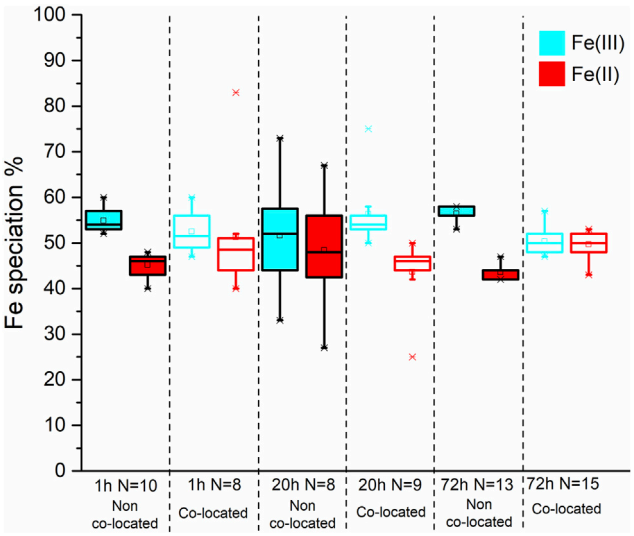

FIGURE 10 | Box and whisker plot diagrams showing the changes in Fe speciation over the course of the experiment. The box and whisker plots for the starting material have a dotted outline. The box and whisker plots from the non co-located regions have a solid black outline while those from the co-located regions have coloured outline. In both spatial regions the Fe(III) and Fe(II) data is represented with blue and red, respectively.

heterogeneity within the sample that the bulk data was unable to detect.

Both the bulk and aggregate Fe $L_{2,3}$ edge data showed a significant early increase in Fe(II) (**Table 3**) suggesting rapid Fe(III) reduction (Roden and Zachara, 1996; Thamdrup, 2000; Hansel et al., 2003; Han et al., 2018; Newsome et al., 2018). However, the aggregate SXM data detected more Fe(II) compared to the bulk data again demonstrating the ability of the aggregate SXM data to highlight heterogeneities within the samples. Given the limited extent of metal solubilisation and therefore the high degree of metal retention in the solid phase, the trends observed in the XAS data are likely representative of the behaviour of the majority of the Fe and Co present in the experiment.

A Greater Proportion of Cobalt Reduction Occurred in the Localised Cell Environment

Between 1 and 20 h (**Figures 3A–F**), mineral phases were closely associated with the cell surface, where outer membrane *c*-type cytochromes, previously implicated in metal reduction, are located (Lovley et al., 2004; MacDonald et al., 2011; Malvankar et al., 2011; Levar et al., 2016; Newsome et al., 2018). Furthermore, in regions where bacteria and mineral were co-located, significantly more Co(II) was detected suggesting the possibility of highly localised enzymatic Co(III) reduction. The proximity between the cells and mineral phases, and the localised increase in Co(II) is consistent with outer membrane cytochromes mediating the reductive transformation of insoluble metal phases directly. At 72 h the reduced mineral phase was distanced from the cell surface (**Figures 3G,H**), indicating the reducibility of the mineral phases had been exhausted with time. The nanoscale Co $L_{2,3}$ edge SXM data highlighted higher standard deviations and broader spreads of data in co-located regions (**Figure 9**, **Supplementary Table S2**) indicating that cells had a varying metabolic potential and therefore identifying heterogeneity within the system. Fe $L_{2,3}$ edge SXM data at the nano scale indicated no spatial changes in Fe speciation from 1 h as the Fe(II):Fe(III) ratio in the system had spatially stabilised whilst the Co(II):Co(III) ratio was still evolving.

CONCLUSION

This work improves our fundamental molecular-scale understanding of the fate of Co in complex environmental systems and supports the development of Co bioprocessing and remediation options in the future. The solid phase retention, alongside the highly localised and preferential cobalt bioreduction observed at the nanoscale is consistent with retention of Co in sediment redox zones, while the Co-magnetite end product of bioreduction in these laboratory experiments has potential industrial applications from drug delivery systems to magnetic recording media.

DATA AVAILABILITY STATEMENT

The raw data supporting the conclusion of this article will be made available by the authors, without undue reservation.

AUTHOR CONTRIBUTIONS

DB, LN, JL and VC contributed to conception and design of the study. DB performed with bulk of the data collection with MK,

BK, TA, VC (SXM), JW (XRD), HB (TEM), AN and VC (XAS and XMCD). DB performed the bulk of the data analysis with assistance from MK, BK, TA (SXM), JW (XRD), and GL (XAS and XMCD). DB wrote the first draft of the manuscript. JL, LN, and VC assisted with extensive manuscript review. All authors contributed to manuscript revision, read, and approved the submitted version.

FUNDING

This work was supported by the Natural Environment Research Council (CoG3 NE/M011518/1) and an EPSRC studentship (Project reference 1919159), the financial support through this project is greatly acknowledged. The Advanced Light Source is supported by the Director, Office of Science, Office of Basic Energy Sciences, of the United States Department of Energy under Contract No. DE-AC02-05CH11231. Beamtime on the Scanning X-Ray Microscopy beamline I08 at the Diamond Light Source was obtained under proposal number SP17626.

SUPPLEMENTARY MATERIAL

The Supplementary Material for this article can be found online at: https://www.frontiersin.org/articles/10.3389/feart.2022.799328/full#supplementary-material

REFERENCES

Agency for Toxic Substances and Disease Registry (2004). *Toxicological Profile for Cobalt*.

Atkins, A. L., Shaw, S., and Peacock, C. L. (2014). Nucleation and Growth of Todorokite from Birnessite: Implications for Trace-Metal Cycling in marine Sediments. *Geochimica et Cosmochimica Acta* 144, 109–125. doi:10.1016/j.gca.2014.08.014

Banakar, V. K. (2010). Deep-sea Ferromanganese Deposits and Their Resource Potential for India. *J. Indian Inst. Sci.* 90 (4), 535–541. doi:10.1016/j.yqres.2010.02.002

Borch, T., Kretzschmar, R., Kappler, A., Cappellen, P. V., Ginder-Vogel, M., Voegelin, A., et al. (2010). Biogeochemical Redox Processes and Their Impact on Contaminant Dynamics. *Environ. Sci. Technol.* 44 (1), 15–23. doi:10.1021/es9026248

Bourdelle, F., Benzerara, K., Beyssac, O., Cosmidis, J., Neuville, D. R., Brown, G. E., et al. (2013). Quantification of the Ferric/Ferrous Iron Ratio in Silicates by Scanning Transmission X-ray Microscopy at the Fe $L_{2,3}$ Edges to Cite This Version : HAL Id : Hal-02270197. *Contrib. Mineralogy Petrol.* 166 (2), 423–434. doi:10.1007/s00410-013-0883-4

Bousserrhine, N., Gasser, U. G., Jeanroy, E., and Berthelin, J. (1999). Bacterial and Chemical Reductive Dissolution of Mn-, Co-, Cr-, and Al-Substituted Goethites. *Geomicrobiology J.* 16 (3), 245–258. doi:10.1080/014904599270622

Burlet, C., and Vanbrabant, Y. (2015). Study of the Spectro-Chemical Signatures of Cobalt-Manganese Layered Oxides (Asbolane-lithiophorite and Their Intermediates) by Raman Spectroscopy. *J. Raman Spectrosc.* 46 (10), 941–952. doi:10.1002/jrs.4755

Byrne, J. M., Coker, V. S., Moise, S., Wincott, P. L., Vaughan, D. J., Tuna, F., et al. (2013). Controlled Cobalt Doping in Biogenic Magnetite Nanoparticles. *J. R. Soc. Interf.* 10, 20130134. doi:10.1098/rsif.2013.0134

Caccavo, F., Lonergan, D. J., Lovley, D. R., Davis, M., Stolz, J. F., and McInerney, M. J. (1994). Geobacter Sulfurreducens Sp. nov., a Hydrogen- and Acetate-Oxidizing Dissimilatory Metal-Reducing Microorganism. *Appl. Environ. Microbiol.* 60 (10), 3752–3759. doi:10.1128/aem.60.10.3752-3759.1994

Chao, W., Fischer, P., Tyliszczak, T., Rekawa, S., Anderson, E., and Naulleau, P. (2012). Real Space Soft X-ray Imaging at 10 Nm Spatial Resolution. *Opt. Express* 20 (9), 9777. doi:10.1364/oe.20.009777

Cismasu, A. C., Williams, K. H., and Nico, P. S. (2016). Iron and Carbon Dynamics during Aging and Reductive Transformation of Biogenic Ferrihydrite. *Environ. Sci. Technol.* 50 (1), 25–35. doi:10.1021/acs.est.5b03021

Cody, G. D., Ade, H., Alexander, M. O. D., Araki, T., Butterworth, A., Fleckenstein, H., et al. (2008). Quantitative Organic and Light-Element Analysis of Comet 81P/Wild 2 Particles Using C-, N-, and O-μ-XANES. *Meteoritics Planet. Sci.* 43 (1–2), 353–365. doi:10.1111/j.1945-5100.2008.tb00627.x

Coker, V. S., Byrne, J. M., Telling, N. D., van der Laan, G., Lloyd, J. R., Hitchcock, A. P., et al. (2012). Characterisation of the Dissimilatory Reduction of Fe(III)-oxyhydroxide at the Microbe - mineral Interface: The Application of STXM-XMCD. *Geobiology* 10, 347–354. doi:10.1111/j.1472-4669.2012.00329.x

Coker, V. S., Pearce, C. I., Lang, C., van der Laan, G., Pattrick, R. A. D., Telling, N. D., et al. (2007). Cation Site Occupancy of Biogenic Magnetite Compared to Polygenic Ferrite Spinels Determined by X-ray Magnetic Circular Dichroism. *Eur. J. Mineral.* 19, 707–716. doi:10.1127/0935-1221/2007/0019-1758

Coker, V. S., Telling, N. D., van der Laan, G., Pattrick, R. A. D., Pearce, C. I., Arenholz, E., et al. (2009). Harnessing the Extracellular Bacterial Production of Nanoscale Cobalt Ferrite with Exploitable Magnetic Properties. *ACS Nano* 3 (7), 1922–1928. doi:10.1021/nn900293d

Cornell, R. M., and Giovanoli, R. (1989). Effect of Cobalt on the Formation of Crystalline Iron Oxides from Ferrihydrite in Alkaline media. *Clays and Clay Minerals* 37 (1), 65–70. doi:10.1346/CCMN.1989.0370108

Cornell, R. M., and Schwertmann, U. (2003). *The Iron Oxides: Structure, Reactions, Occurences and Uses*. Hoboken, New Jersey: Wiley VCH.

Dehaine, Q., Tijsseling, L. T., Glass, H. J., Törmänen, T., and Butcher, A. R. (2021). Geometallurgy of Cobalt Ores: A Review. *Minerals Eng.* 160, 106656. doi:10.1016/j.mineng.2020.106656

European Commission (2017). "Communication from the Commission to the European Parliament, the Council, the Eurpean Economic and Social Committee and the Committee of the Regions on the 2017 List of Critical Raw Materials for the EU," in *Official Journal of the European Union* (Brussels: COM), 8.

Faucon, M.-P., Shutcha, M. N., and Meerts, P. (2007). Revisiting Copper and Cobalt Concentrations in Supposed Hyperaccumulators from SC Africa: Influence of Washing and Metal Concentrations in Soil. *Plant Soil* 301 (1–2), 29–36. doi:10.1007/s11104-007-9405-3

Fredrickson, J. K., Zachara, J. M., Kukkadapu, R. K., Gorby, Y. A., Smith, S. C., and Brown, C. F. (2001). Biotransformation of Ni-Substituted Hydrous Ferric Oxide by an Fe(III)-reducing Bacterium. *Environ. Sci. Technol.* 35 (4), 703–712. doi:10.1021/es001500v

Glatzel, P., Yano, J., Bergmann, U., Visser, H., Robblee, J. H., Gu, W., et al. (2005). Resonant Inelastic X-ray Scattering (RIXS) Spectroscopy at the Mn K Absorption Pre-edge-a Direct Probe of the 3d Orbitals. *J. Phys. Chem. Sol.* 66 (12), 2163–2167. doi:10.1016/j.jpcs.2005.09.012

Gorby, Y. A., Caccavo, F., and Bolton, H. (1998). Microbial Reduction of CobaltIIIEDTA- in the Presence and Absence of Manganese(IV) Oxide. *Environ. Sci. Technol.* 32 (2), 244–250. doi:10.1021/es970516r

Grybos, M., Davranche, M., Gruau, G., and Petitjean, P. (2007). Is Trace Metal Release in Wetland Soils Controlled by Organic Matter Mobility or Fe-Oxyhydroxides Reduction? *J. Colloid Interf. Sci.* 314 (2), 490–501. doi:10.1016/j.jcis.2007.04.062

Han, R., Liu, T., Li, F., Li, X., Chen, D., and Wu, Y. (2018). Dependence of Secondary Mineral Formation on Fe(II) Production from Ferrihydrite Reduction by Shewanella Oneidensis MR-1. *ACS Earth Space Chem.* 2 (4), 399–409. doi:10.1021/acsearthspacechem.7b00132

Hansel, C. M., Benner, S. G., Neiss, J., Dohnalkova, A., Kukkadapu, R. K., and Fendorf, S. (2003). Secondary Mineralization Pathways Induced by Dissimilatory Iron Reduction of Ferrihydrite under Advective Flow. *Geochimica et Cosmochimica Acta* 67 (16), 2977–2992. doi:10.1016/S0016-7037(03)00276-X

Hawkings, J. R., Benning, L. G., Raiswell, R., Kaulich, B., Araki, T., Abyaneh, M., et al. (2018). Biolabile Ferrous Iron Bearing Nanoparticles in Glacial Sediments. *Earth Planet. Sci. Lett.* 493, 92–101. doi:10.1016/j.epsl.2018.04.022

He, Y., Liu, X., Chen, G., Pan, J., Yan, A., Li, A., et al. (2020). Synthesis of Co(II)-Fe(III) Hydroxide Nanocones with Mixed Octahedral/Tetrahedral Coordination toward Efficient Electrocatalysis. *Chem. Mater.* 32 (10), 4232–4240. doi:10.1021/acs.chemmater.0c00512

Hein, J. R., and Koschinsky, A. (2014). "Deep-Ocean Ferromanganese Crusts and Nodules," in *Treatise on Geochemistry*. 2nd edn (Amsterdam: Elsevier), 273–291. doi:10.1016/B978-0-08-095975-7.01111-6

Hein, J. R., Spinardi, F., Okamoto, N., Mizell, K., Thorburn, D., and Tawake, A. (2015). Critical Metals in Manganese Nodules from the Cook Islands EEZ, Abundances and Distributions. *Ore Geology. Rev.* 68, 97–116. doi:10.1016/j.oregeorev.2014.12.011

Hitchcock, A. P. (2011). No Title. Available at: http://unicorn.mcmaster.ca/aXis2000.html.

Istomin, S. Y., Tyablikov, O. A., Kazakov, S. M., Antipov, E. V., Kurbakov, A. I., Tsirlin, A. A., et al. (2015). An Unusual High-Spin Ground State of Co3+ in Octahedral Coordination in Brownmillerite-type Cobalt Oxide. *Dalton Trans.* 44 (23), 10708–10713. doi:10.1039/c4dt03670k

Jacobsen, C., Wirick, S., Flynn, G., and Zimba, C. (2000). Soft X-ray Spectroscopy from Image Sequences with Sub-100 Nm Spatial Resolution. *J. Microsc.* 197 (2), 173–184. doi:10.1046/j.1365-2818.2000.00640.x

Joshi, N., Filip, J., Coker, V. S., Sadhukhan, J., Safarik, I., Bagshaw, H., et al. (2018). Microbial Reduction of Natural Fe(III) Minerals; toward the Sustainable Production of Functional Magnetic Nanoparticles. *Front. Environ. Sci.* 6 (NOV), 1–11. doi:10.3389/fenvs.2018.00127

Josso, P., Pelleter, E., Pourret, O., Fouquet, Y., Etoubleau, J., Cheron, S., et al. (2017). A New Discrimination Scheme for Oceanic Ferromanganese Deposits Using High Field Strength and Rare Earth Elements. *Ore Geology. Rev.* 87, 3–15. doi:10.1016/j.oregeorev.2016.09.003

Kappler, A., Bryce, C., Mansor, M., Lueder, U., Byrne, J. M., and Swanner, E. D. (2021). An Evolving View on Biogeochemical Cycling of Iron. *Nat. Rev. Microbiol.*, 19, 360–374. (iii). doi:10.1038/s41579-020-00502-7

Karunakaran, C., Christensen, C. R., Gaillard, C., Lahlali, R., Blair, L. M., Perumal, V., et al. (2015). Introduction of Soft X-ray Spectromicroscopy as an Advanced Technique for Plant Biopolymers Research. *PLoS ONE* 10 (3), e0122959–18. doi:10.1371/journal.pone.0122959

Kosiorek, M., and Wyszkowski, M. (2019). Effect of Cobalt on the Environment and Living Organisms - A Review. *Appl. Ecol. Env. Res.* 17 (5), 11419–11449. doi:10.15666/aeer/1705_1141911449

Kukkadapu, R. K., Zachara, J. M., Fredrickson, J. K., and Kennedy, D. W. (2004). Biotransformation of Two-Line Silica-Ferrihydrite by a Dissimilatory Fe(III)-reducing Bacterium: Formation of Carbonate green Rust in the Presence of Phosphate. *Geochimica et Cosmochimica Acta* 68 (13), 2799–2814. doi:10.1016/j.gca.2003.12.024

Lawrence Berkeley National Laboratory (2021). Advanced Light Soruce, Magnetic Spectroscopy/Materials Science. Endstation 6.3.1 - Magnetic Spectroscopy and Mapping. Available at: https://als.lbl.gov/beamlines/6-3-1/(Accessed: July 30, 2021).

Lawrence, J. R., Swerhone, G. D. W., Leppard, G. G., Araki, T., Zhang, X., West, M. M., et al. (2003). Scanning Transmission X-ray, Laser Scanning, and Transmission Electron Microscopy Mapping of the Exopolymeric Matrix of Microbial Biofilms. *Appl. Environ. Microbiol.* 69, 5543–5554. doi:10.1128/AEM.69.9.5543-5554.2003

Lee, E. Y., Noh, S.-R., Cho, K.-S., and Ryu, H. W. (2001). Leaching of Mn, Co, and Ni from Manganese Nodules Using an Anaerobic Bioleaching Method. *J. Biosci. Bioeng.* 92 (4), 354–359. doi:10.1016/S1389-1723(01)80239-5

Levar, C. E., Hoffman, C. L., Dunshee, A. J., Toner, B. M., and Bond, D. R. (2016). Redox Potential as a Master Variable Controlling Pathways of Metal Reduction byGeobacter Sulfurreducens. *ISME J.* 11, 741–752. doi:10.1101/043059

Li, X., Liu, T., Li, F., Zhang, W., Zhou, S., and Li, Y. (2012). Reduction of Structural Fe(III) in Oxyhydroxides by Shewanella Decolorationis S12 and Characterization of the Surface Properties of Iron Minerals. *J. Soils Sediments* 12 (2), 217–227. doi:10.1007/s11368-011-0433-5

Lloyd, J. R. (2003). Microbial Reduction of Metals and Radionuclides. *FEMS Microbiol. Rev.* 27 (27), 411–425. doi:10.1016/S0168-6445(03)00044-5

López, J. L., Pfannes, H.-D., Paniago, R., Sinnecker, J. P., and Novak, M. A. (2008). Investigation of the Static and Dynamic Magnetic Properties of CoFe2O4 Nanoparticles. *J. Magnetism Magn. Mater.* 320 (14), e327–e330. doi:10.1016/j.jmmm.2008.02.065

Lovley, D. R., Holmes, D. E., and Nevin, K. P. (2004). Dissimilatory Fe(III) and Mn(IV) Reduction. *Adv. Microb. Physiol.* 49, 219–286. doi:10.1016/S0065-2911(04)49005-5

Lovley, D. R. (1987). Organic Matter Mineralization with the Reduction of Ferric Iron: A Review. *Geomicrobiology J.* 5 (3–4), 375–399. doi:10.1080/01490458709385975

Lovley, D. R., Stolz, J. F., Nord, G. L., and Phillips, E. J. P. (1987). Anaerobic Production of Magnetite by a Dissimilatory Iron-Reducing Microorganism. *Nature* 330, 252–254. doi:10.1038/330252a0

Lovley, D. R., and Walker, D. J. F. (2019). Geobacter Protein Nanowires. *Front. Microbiol.* 10 (September). doi:10.3389/fmicb.2019.02078

Ma, R., Takada, K., Fukuda, K., Iyi, N., Bando, Y., and Sasaki, T. (2008). Topochemical Synthesis of Monometallic (Co2+-Co3+) Layered Double Hydroxide and its Exfoliation into Positively Charged Co(OH)2 Nanosheets. *Angew. Chem. Int. Ed.* 47 (1), 86–89. doi:10.1002/anie.200703941

MacDonald, L. H., Moon, H. S., and Jaffé, P. R. (2011). The Role of Biomass, Electron Shuttles, and Ferrous Iron in the Kinetics of Geobacter Sulfurreducens-Mediated Ferrihydrite Reduction. *Water Res.* 45 (3), 1049–1062. doi:10.1016/j.watres.2010.10.017

Maciąg, Ł., Zawadzki, D., Kozub-Budzyń, G. A., Piestrzyński, A., Kotliński, R. A., and Wróbel, R. J. (2019). Mineralogy of Cobalt-Rich Ferromanganese Crusts from the Perth Abyssal plain (E Indian Ocean). *Minerals* 9 (2), 84. doi:10.3390/min9020084

Malvankar, N. S., Vargas, M., Nevin, K. P., Franks, A. E., Leang, C., Kim, B.-C., et al. (2011). Tunable Metallic-like Conductivity in Microbial Nanowire Networks. *Nat. Nanotech* 6, 573–579. doi:10.1038/nnano.2011.119

Manceau, A., Manceau, A., and Gates, W. P. (1997). Surface Structural Model for Ferrihydrite. *Clays and Clay Minerals* 45 (3), 448–460. doi:10.1346/CCMN.1997.0450314

Marsh, E., Anderson, E., and Gray, F. (2013). "Nickel-Cobalt Laterites—A Deposit Model," in *Mineral Deposit Models for Resource Assessment*. Reston: USGS, 49.

Mizell, K., and Hein, J. R. (2018). "Ferromanganese Crusts and Nodules: Rocks that Grow," in *Encyclopedia of Earth Sciences Series*. Cham: Springer, 477–483. doi:10.1007/978-3-319-39312-4_101

Moffet, R. C., Tivanski, A. V., and Gilles, M. K. (2011). *Scanning Transmission X-ray Microscopy: Applications in Atmospheric Aerosol Research*. Berkeley, California: Lawrence Berkeley National Laboratory. Available at: https://www.osti.gov/servlets/purl/1005004 (Accessed: March 9, 2021).

Mohwinkel, D., Kleint, C., and Koschinsky, A. (2014). Phase Associations and Potential Selective Extraction Methods for Selected High-Tech Metals from Ferromanganese Nodules and Crusts with Siderophores. *Appl. Geochem.* 43 (April), 13–21. doi:10.1016/j.apgeochem.2014.01.010

Naden, J. (2017). *Science and Implementation Plan Security of Supply of Mineral Resources*. Nottingham: SoS Minerals. Research Programme EXPERT GROUP.

Newsome, L., Lopez Adams, R., Downie, H. F., Moore, K. L., and Lloyd, J. R. (2018). NanoSIMS Imaging of Extracellular Electron Transport Processes during Microbial Iron(III) Reduction. *FEMS Microbiol. Ecol.* 94 (8), 1–13. doi:10.1093/femsec/fiy104

Newsome, L., Solano Arguedas, A., Coker, V. S., Boothman, C., and Lloyd, J. R. (2020). Manganese and Cobalt Redox Cycling in Laterites; Biogeochemical and Bioprocessing Implications. *Chem. Geology.* 531, 119330. doi:10.1016/j.chemgeo.2019.119330

Nitahara, S., Kato, S., Usui, A., Urabe, T., Suzuki, K., and Yamagishi, A. (2017). Archaeal and Bacterial Communities in Deep-Sea Hydrogenetic Ferromanganese Crusts on Old Seamounts of the Northwestern Pacific. *PLoS ONE* 12 (2), e0173071–21. doi:10.1371/journal.pone.0173071

Pattrick, R. A. D., van der Laan, G., Henderson, C. M. B., Kuiper, P., Dudzik, E., and Vaughan, D. J. (2002). Cation Site Occupancy in Spinel Ferrites Studied by X-ray Magnetic Circular Dichroism: Developing a Method for Mineralogists. *Eur. J. Mineral.* 14, 1095–1102. doi:10.1127/0935-1221/2002/0014-1095

Petavratzi, C. E., Gunn, G., and Kresse, C. (2019). BGS Commodity Review Cobalt. Available at: https://www.bgs.ac.uk/mineralsuk/whatsnew.html#cobalt.

Poggenburg, C., Mikutta, R., Sander, M., Schippers, A., Marchanka, A., Dohrmann, R., et al. (2016). Microbial Reduction of Ferrihydrite-Organic Matter

Coprecipitates by Shewanella Putrefaciens and Geobacter Metallireducens in Comparison to Mediated Electrochemical Reduction. *Chem. Geology.* 447, 133–147. doi:10.1016/j.chemgeo.2016.09.031

Pollock, T. M. (2016). Alloy Design for Aircraft Engines. *Nat. Mater* 15, 809–815. doi:10.1038/nmat4709

Pozas, R., Rojas, T. C., Ocaña, M., and Serna, C. J. (2004). The Nature of Co in Synthetic Co-substituted Goethites. *Clays Clay Miner.* 52 (6), 760–766. doi:10.1346/CCMN.2004.0520611

Roden, E. E., and Zachara, J. M. (1996). Microbial Reduction of Crystalline Iron(III) Oxides: Influence of Oxide Surface Area and Potential for Cell Growth. *Environ. Sci. Technol.* 30 (5), 1618–1628. doi:10.1021/es9506216

Sharma, R. K., and Agrawal, M. (2005). Biological Effects of Heavy Metals: An Overview. *J. Environ. Biol.* 26 (2 Suppl. L), 301–313.

Shedd, K. B. (2015). "2015 Minerals Yearbook - Cobalt," in *USGS Mineral Resources Program*. Reston: USGS, 20. Available at: https://minerals.usgs.gov/minerals/pubs/commodity/cobalt/myb1-2015-cobal.pdf%0Ahttp://minerals.usgs.gov/minerals/pubs/commodity/soda_ash/myb1-2015-sodaa.pdf.

Slack, J. F., Kimball, B. E., and Shedd, K. B. (2017). *Cobalt Critical Mineral Resources of the United States — Economic and Environmental Geology and Prospects for Future Supply*. Reston: USGS, F1–F40. *Professional Paper 1802-F*. Available at: .https://doi.org/10.3133/pp1802F

Smith, C. G. (2001). Always the Bridesmaid, Never the Bride: Cobalt Geology and Resources. *Appl. Earth Sci.* 110 (MAY/AUG), 75–80. Transactions of the Institutions of Mining and Metallurgy, Section B: Applied Earth Science. doi:10.1179/aes.2001.110.2.75

Stookey, L. L. (1970). Ferrozine---a New Spectrophotometric Reagent for Iron. *Anal. Chem.* 42, 779–781. doi:10.1021/ac60289a016

Thamdrup, B. (2000). "Bacterial Manganese and Iron Reduction in Aquatic Sediments," in *Advances in Microbial Ecology*, 41–84. doi:10.1007/978-1-4615-4187-5_2

Tkaczyk, A. H., Bartl, A., Amato, A., Lapkovskis, V., and Petranikova, M. (2018). Sustainability Evaluation of Essential Critical Raw Materials: Cobalt, Niobium, Tungsten and Rare Earth Elements. *J. Phys. D: Appl. Phys.* 51 (20), 203001. doi:10.1088/1361-6463/aaba99

Valsangkar, A. B., Khadge, N. H., and Erwin Desa, J. A. (1992). Geochemistry of Polymetallic Nodules from the Central Indian Ocean Basin. *Marine Geol.* 103, 361–371. doi:10.1016/0025-3227(92)90026-E

van der Laan, G., and Kirkman, I. (1992). The 2p Absorption Spectra of 3d Transition Metal Compounds in Tetrahedral and Octahedral Symmetry. *J. Phys. Condensed Matter* 4, 4189–4204. doi:10.1088/0953-8984/4/16/019

van der Laan, G., and Thole, B. T. (1991). Strong Magnetic X-ray Dichroism in 2pabsorption Spectra of 3dtransition-Metal Ions. *Phys. Rev. B* 43 (16), 13401–13411. doi:10.1103/physrevb.43.13401

Vanbrabant, Y., Burlet, C., and Louis, P. (2013). "Mineralogical Characterization of Cobaltic Oxides from the Democratic Republic of Congo," in *TMS Annual Meeting*. Springer, Cham, 243–254. doi:10.1002/9781118658826.ch17

Weber, K. A., Achenbach, L. A., and Coates, J. D. (2006). Microorganisms Pumping Iron: Anaerobic Microbial Iron Oxidation and Reduction. *Nat. Rev. Microbiol.* 4 (10), 752–764. doi:10.1038/nrmicro1490

Wu, N.-L., Kuo, S.-L., Lee, J.-F., and Sheu, H.-S. (2007). Investigation on Pseudocapacitance Mechanism of MFe2O4 Supercapacitors. In: MAterials Chemistry. *National Synchrotron Radiation Research Center (NSRRC)*. Hsinchu, Taiwan.

Woodward, G. L., Peacock, C. L., Otero-Fariña, A., Thompson, O. R., Brown, A. P., and Burke, I. T. (2018). A Universal Uptake Mechanism for Cobalt(II) on Soil Constituents: Ferrihydrite, Kaolinite, Humic Acid, and Organo-mineral Composites. *Geochimica et Cosmochimica Acta* 238, 270–291. doi:10.1016/j.gca.2018.06.035

Xia, J.-L., Liu, H.-C., Nie, Z.-Y., Peng, A.-A., Zhen, X.-J., Yang, Y., et al. (2013). Synchrotron Radiation Based STXM Analysis and Micro-XRF Mapping of Differential Expression of Extracellular Thiol Groups by Acidithiobacillus Ferrooxidans Grown on Fe2+ and S0. *J. Microbiol. Methods* 94 (3), 257–261. doi:10.1016/j.mimet.2013.06.030

Yang, K., Peng, H., Wen, Y., and Li, N. (2010). Re-examination of Characteristic FTIR Spectrum of Secondary Layer in Bilayer Oleic Acid-Coated Fe3O4 Nanoparticles. *Appl. Surf. Sci.* 256 (10), 3093–3097. doi:10.1016/j.apsusc.2009.11.079

Yee, N., Shaw, S., Benning, L. G., and Nguyen, T. H. (2006). The Rate of Ferrihydrite Transformation to Goethite via the Fe(II) Pathway. *Am. Mineral.* 91 (1), 92–96. doi:10.2138/am.2006.1860

Zachara, J. M., Fredrickson, J. K., Smith, S. C., and Gassman, P. L. (2001). Solubilization of Fe(III) Oxide-Bound Trace Metals by a Dissimilatory Fe(III) Reducing Bacterium. *Geochimica et Cosmochimica Acta* 65 (1), 75–93. doi:10.1016/S0016-7037(00)00500-7

Zhang, W., and Cheng, C. Y. (2007). Manganese Metallurgy Review. Part II: Manganese Separation and Recovery from Solution. *Hydrometallurgy* 89, 160–177. doi:10.1016/j.hydromet.2007.08.009

Conflict of Interest: The authors declare that the research was conducted in the absence of any commercial or financial relationships that could be construed as a potential conflict of interest.

Publisher's Note: All claims expressed in this article are solely those of the authors and do not necessarily represent those of their affiliated organizations, or those of the publisher, the editors, and the reviewers. Any product that may be evaluated in this article, or claim that may be made by its manufacturer, is not guaranteed or endorsed by the publisher.